

Crash-testing the CAULDRON code for joint lensing and dynamics analysis of early-type galaxies

Matteo Barnabè¹*, Carlo Nipoti², Léon V. E. Koopmans¹, Simona Vegetti¹ and Luca Ciotti²

¹*Kapteyn Astronomical Institute, University of Groningen, PO Box 800, 9700 AV Groningen, the Netherlands*

²*Astronomy Department, University of Bologna, via Ranzani 1, 40127 Bologna, Italy*

Published as MNRAS 393, 1114

ABSTRACT

We apply the joint lensing and dynamics code for the analysis of early-type galaxies, “CAULDRON”, to a rotating N-body stellar system with dark matter halo which significantly violates the two major assumptions of the method, i.e. axial symmetry supported by a two-integral distribution function. The goal is to study how CAULDRON performs in an extreme case, and to determine which galaxy properties can still be robustly recovered. Three data sets, corresponding to orthogonal lines of sight, are generated from the N-body system and analysed with the identical procedure followed in the study of real lens galaxies, adopting an axisymmetric power-law total density distribution. We find that several global properties of the N-body system are recovered with remarkable accuracy, despite the fact that the adopted power-law model is too simple to account for the lack of symmetry of the true density distribution. In particular, the logarithmic slope of the total density distribution is robustly recovered to within less than 10% (with the exception of the ill-constrained very inner regions), the inferred angle-averaged radial profile of the total mass closely follows the true distribution, and the dark matter fraction of the system (inside the effective radius) is correctly determined within $\sim 10\%$ of the total mass. Unless the line of sight direction is almost parallel to the total angular momentum vector of the system, reliably recovered quantities also include the angular momentum, the V/σ ratio, and the anisotropy parameter δ . We conclude that the CAULDRON code can be safely and effectively applied to real early-type lens galaxies, providing reliable information also for systems that depart significantly from the method’s assumptions.

Key words: gravitational lensing — methods: N-body simulations — galaxies: elliptical and lenticular, cD — galaxies: kinematics and dynamics — galaxies: structure.

1 INTRODUCTION

Determining the structure of early-type galaxies and reliably pinning down their dark matter content is a crucial step in order to fully understand the formation and evolution processes of these systems.

Within the currently favoured cosmological scenario, the Λ CDM paradigm, early-type galaxies are thought to be formed via hierarchical merging of lower mass galaxies (Toomre 1977; White & Frenk 1991; Barnes 1992; Cole et al. 2000). While very successful in reproducing many observational features of elliptical galaxies, including complex ones (see e.g. Jesseit et al. 2007), these formation models are still encountering difficulties in explaining the origin of the empirical scaling laws that correlate the global properties of early-type galaxies (see e.g. Robertson et al. 2006). Providing a reliable and detailed description of the mass density distribution, orbital structure and intrinsic properties of early-type

galaxies is therefore critical in order to enable stringent tests of galaxy formation models.

For this reason, considerable effort has been devoted during the last decades towards the observation and the modelization of nearby early-type galaxies, by means of both stellar dynamics and X-ray studies, finding more or less strong evidence for a dark matter halo component (e.g. Fabbiano 1989, Mould et al. 1990, Saglia, Bertin & Stiavelli 1992, Bertin et al. 1994, Franx et al. 1994, Carollo et al. 1995, Arnaboldi et al. 1996, Rix et al. 1997, Matsushita et al. 1998, Loewenstein & White 1999, Gerhard et al. 2001, Borriello et al. 2003, Romanowsky et al. 2003, Humphrey et al. 2006, Forbes et al. 2008 and more recently the SAURON collaboration: see e.g. de Zeeuw et al. 2002, Emsellem et al. 2004, Cappellari et al. 2006). Both methods, however, present some difficulties. In the case of stellar dynamics it is believed that some degeneracy can be present between the mass profile of the galaxy and the anisotropy of the stellar velocity dispersion tensor, which can be alleviated when higher or-

* E-mail: M.Barnabe@astro.rug.nl

der velocity moments are available (see e.g. Gerhard 1993) or by using physically motivated distribution functions (see e.g. Bertin 2000, for a discussion of this point). X-ray analyses, on the other hand, can seriously overestimate the total mass of the system if the assumption of hydrostatic equilibrium for the hot gas does not hold, especially near the center (see e.g. Pellegrini & Ciotti 2006; Ciotti & Pellegrini 2008).

A full understanding of the evolution of early-type galaxies cannot be achieved without extending the study also to the mass density profile of objects at higher redshift ($z \gtrsim 0.1$). This, however, has not been attempted until recently, due to observational limitations and to the increased difficulty in extracting detailed kinematic information, which hinders traditional analyses based on stellar dynamics only. An effective solution in order to overcome these issues is constituted by a joint analysis which combines the constraints from stellar dynamics with the information obtained from gravitational lensing, when the early-type galaxy also happens to act as a lens with respect to a background source at higher redshift (Treu & Koopmans 2002; Koopmans & Treu 2002; Treu & Koopmans 2003, 2004; van de Ven et al. 2008). Koopmans et al. (2006) have successfully used this combined approach to analyse fifteen early-type lens galaxies (within a redshift range $z = 0.06 - 0.33$) discovered in the Sloan Lens ACS Survey (SLACS, Bolton et al. 2006) as well as six systems between $z \sim 0.5$ and 1 from the Lenses Structure and Dynamics (LSD) Survey, showing that all of the examined systems are well described by a power-law total density distribution very close to r^{-2} . The technique for the joint lensing and dynamics analysis has been expanded by Barnabè & Koopmans (2007, hereafter BK07) into a general and self-consistent method, completely embedded within the framework of Bayesian statistics, which puts constraints on the total density distribution of the lens galaxy by taking advantage of all the available data, i.e. not only the lensed image and a single stellar velocity dispersion measurement, but also the surface brightness distribution and the 2D kinematic maps (first and second projected velocity moments).

Similar to other methods for the determination of the structure and internal dynamics of early-type galaxies, already mentioned above, the joint lensing and dynamics analysis also relies on a certain number of assumptions. For example, the simple and robust approach of Koopmans et al. (2006) treats the gravitational lensing and the stellar dynamics as independent problems. The projected mass distribution of the lens galaxy is modelled as a singular isothermal ellipsoid in order to determine the total mass within the Einstein radius, which is then used as a constraint for the dynamical model, where spherical symmetry and a specific prescription for the stellar orbital anisotropy are assumed. The more sophisticated framework of BK07 is designed to be very general and allows in principle for an arbitrary choice of the total potential. In practice, however, such freedom must balance against technical and computational limitations. Therefore, in order to have a fast and efficient algorithm, the current implementation of the method, the CAULDROn code¹, is restricted to axisymmetric potentials and two-integral stellar phase-space distribution functions (DFs). Under these hypotheses, it has been shown in BK07 that the method is capable of recovering with considerable accuracy the correct potential parameters and inclination angle, even in the presence of realistic noise.

The point above raises the question of whether (and to what extent) the simplifying assumptions can be deemed valid for the as-

trophysical systems to which such methods are applied. In fact, real galaxies are not idealized objects, and there is no reason to expect them to be exactly axisymmetric (and neither triaxial ellipsoids) or to have two or three integrals of motion. Whereas axial symmetry generally seems to constitute a fairly good approximate description for most early-type galaxies, a more detailed inspection, such as that allowed by the SAURON observations (see Emsellem et al. 2004; McDermid et al. 2006), reveals a multitude of features indicating departure from axisymmetry, e.g. the presence of isophotal twist in the surface brightness distribution, minor axis rotation and kinematically decoupled cores.

For this reason, in the present paper we apply our algorithm to the end-product of a two-component (stars plus dark matter) N-body simulation of a merger process, i.e. to a system which does not obey any restrictive prescription of symmetry, and therefore violates the assumptions of the method. We aim to study how the CAULDROn algorithm performs when subjected to this kind of “crash-test”, and which quantities can be robustly recovered even in such an extreme case. A similar approach has been followed by Thomas et al. (2007), who have applied their three-integral axisymmetric Schwarzschild code to the study of non axisymmetric N-body merger remnants, although without any gravitational lensing information, and by Meneghetti et al. (2007) in the case of clusters of galaxies.

The paper is organized as follows. In Section 2 we provide an overview of the CAULDROn algorithm for combined lensing and dynamics analysis. In Section 3 we summarize the properties of the N-body system that we use as lens galaxy. In Section 4 we describe how the 2D maps of the simulated data with added realistic noise are obtained from the particle distribution. In Section 5 we apply the joint lensing and dynamics analysis to the simulated data and we present the results, which are then further discussed in Section 6, where also conclusions are drawn.

2 THE CAULDROn ALGORITHM FOR JOINT LENSING AND DYNAMICS ANALYSIS

In this Section we recall the main features of the CAULDROn algorithm. We refer the reader to BK07 for a fully detailed description of the method.

The central tenet of a self-consistent joint analysis is to adopt a total gravitational potential Φ (or, equivalently, the total density profile ρ , from which Φ is calculated via the Poisson equation), parametrized by a set η of non-linear parameters, and use it simultaneously for both the gravitational lensing and the stellar dynamics modelling of the data. As shown in BK07, these two modelling problems, while different from a physical point of view, can be expressed in an analogous way as a single set of coupled (regularized) linear equations. For any given choice of the non-linear parameters, the equations can be solved (in a direct, non-iterative way) to simultaneously obtain as the best solution for the chosen potential model: (i) the unlensed source surface brightness distributions, and (ii) the weights of the elementary stellar dynamics building blocks (e.g. orbits or two-integral components, TICs, Schwarzschild 1979; Verolme & de Zeeuw 2002). This linear optimization scheme is consistently embedded in the framework of Bayesian statistics. As a consequence, it is possible to objectively assess the probability of each model by means of the evidence merit function and, therefore, to rank different models (see Mackay 1992, 1999, 2003). In this way, by maximizing the evidence, it is possible to recover the set of non-linear parameters η corresponding to the “best” potential

¹ Combined Algorithm for Unified Lensing and Dynamics Reconstruction

model. Here, in the context of Bayesian statistics, the “best model” means the most plausible model in an Occam’s razor sense, given the data and the adopted form of the regularization (the optimal level of the regularization is also set by the evidence).

Whereas the method is in principle extremely general², its current practical implementation, which will be referred to as the CAULDRON algorithm, is more restricted in order to make it computationally efficient and applies specifically to axisymmetric potentials, $\Phi(R, z)$, and two-integral DFs $f = f(E, L_z)$ (where E and L_z are, respectively, the energy and the angular momentum along the rotation axis). Under these assumptions, the dynamical model can be constructed by making use of the fast BK07 numerical implementation of the two-integral Schwarzschild method developed by Cretton et al. (1999) and Verolme & de Zeeuw (2002), whose building blocks are not stellar orbits (as in the classical Schwarzschild method) but TICs.³ The weights map of the optimal TIC superposition which best reproduces the observables is yielded as an outcome of the joint analysis.

The CAULDRON algorithm has been successfully tested against the analytic power-law galaxy models of Evans (1994), which respect by construction the assumptions of axisymmetry and two-integral DF, and afterwards has been employed for the detailed analysis of the SLACS lens galaxy SDSS J2321–097 (Czoske et al. 2008, hereafter C08). The latter is a case study which presents a benchmark data set particularly well suited to the needs of CAULDRON, i.e. high-resolution HST/ACS images of the gravitational lensed source and of the surface brightness distribution of the lens galaxy, and 2D maps of the projected velocity moments of the lens galaxy derived from VLT-VIMOS observations. Therefore, the observations of SDSS J2321–097 will be used as a reference in order to generate the simulated observables for the present study (see Section 4).

It has been shown by the work of Koopmans et al. (2006) that a simple power-law model for the total density distribution provides a satisfactory description for all of the SLACS lens galaxies examined so far. This has been further confirmed in the case of SDSS J2321–097, where a fully self-consistent analysis was performed. In the present work, we aim to study the simulated galaxies exactly as we would do for real objects, without assuming any a priori knowledge, and therefore we still adopt the same power-law model that has been used in C08. In particular, the total mass density distribution of the galaxy is taken to be a power-law stratified on axisymmetric homoeoids:

$$\rho(m) = \frac{\rho_0}{m^{\gamma'}}, \quad 0 < \gamma' < 3, \quad (1)$$

where ρ_0 is a density scale, γ' will be referred to as the (logarithmic) slope of the density profile, and

$$m^2 = \frac{R^2}{a_0^2} + \frac{z^2}{c_0^2} = \frac{R^2}{a_0^2} + \frac{z^2}{a_0^2 q^2}, \quad (2)$$

where c_0 and a_0 are length-scales and $q \equiv c_0/a_0$.

² One could adopt for example a completely general pixelized potential for which the best profile is then determined via Bayesian statistics only by the data.

³ A TIC can be visualized as an elementary toroidal system, completely specified by a particular choice of energy E and axial component of the angular momentum L_z . TICs have simple $1/R$ radial density distributions and analytic unprojected velocity moments, and by superposing them one can build $f(E, L_z)$ models for arbitrary spheroidal potentials (cf. Cretton et al. 1999): all these characteristics contribute to make TICs particularly valuable and “inexpensive” building blocks when compared to orbits.

The (inner) gravitational potential associated with a homoeoidal density distribution $\rho(m)$ is given by Chandrasekhar (1969) formula. In our case, for $\gamma' \neq 2$, one has

$$\Phi(R, z) = -\frac{\Phi_0}{\gamma' - 2} \int_0^\infty \frac{\tilde{m}^{2-\gamma'}}{(1+\tau) \sqrt{q^2 + \tau}} d\tau, \quad (3)$$

while for $\gamma' = 2$

$$\Phi(R, z) = \Phi_0 \int_0^\infty \frac{\log \tilde{m}}{(1+\tau) \sqrt{q^2 + \tau}} d\tau, \quad (4)$$

where $\Phi_0 = 2\pi G q a_0^2 \rho_0$ and

$$\tilde{m}^2 = \frac{R^2}{a_0^2(1+\tau)} + \frac{z^2}{a_0^2(q^2 + \tau)}. \quad (5)$$

There are three free non-linear parameters in the potential to be determined via the evidence maximization: Φ_0 (or equivalently, through equation [B4] of BK07, the lens strength α_0), the slope γ' and the axial ratio q . When required by the data, it is straightforward to include a core radius R_s in the density distribution. Beyond the previously mentioned parameters, there are four additional parameters which determine the geometry of the observed system: the position angle ϑ_{PA} , the inclination i and the coordinates of the centre of the lens galaxy with respect to the sky grid. The position angle and the lens center can usually be accurately determined by means of a preliminary exploration and kept fixed afterwards in order to reduce the number of free parameters. Finally, for a proper modelling of the lensed image it can be necessary to include two more parameters (shear strength ζ and shear angle ϑ_ζ) in order to account for external shear.

A curvature regularization (as described in Suyu et al. 2006 and appendix A of BK07) is adopted for both the gravitational lensing and the stellar dynamics reconstructions. As discussed in BK07, the initial guess values of the hyperparameters (defining the level of the regularization) are chosen to be quite large, since the convergence to the maximum is faster when starting from an over-regularized system.

3 THE N-BODY SYSTEM

The model galaxy that we use as lens in the present work is the end-product of a numerical N-body simulation of a dissipationless merging between two equal-mass spherical galaxies embedded in their dark matter halos. The simulation, run with the treecode FVFPs (Fortran Version of a Fast Poisson Solver; Londrillo, Nipoti & Ciotti 2003; Nipoti, Londrillo & Ciotti 2003), has been already presented and described in a previous paper (Nipoti, Londrillo & Ciotti 2007), in which it is named E25o. Here we recall the main properties of the end-product of this simulation, while we refer the reader to Nipoti et al. (2007) for a detailed description of the initial conditions.

The simulation end-product is a nearly ellipsoidal virialized system, comprising a stellar component and a dark-matter component. The total number of particles is $\sim 1.2 \times 10^6$, and all particles have the same mass. The stellar component has total mass $\sim 2 M_*$ and angle-averaged half-mass radius $\sim 3.8 r_*$, where M_* and r_* are the code length and mass unit. The dark matter component is more massive and more extended than the stellar component, having mass $\sim 10 M_*$ and half mass radius $\sim 19.3 r_*$. The system has a virial velocity dispersion $\sim 0.55(GM_*/r_*)^{1/2}$ and non-vanishing total angular momentum \mathbf{L} , corresponding to a value $\lambda \sim 0.07$ in terms of the spin parameter $\lambda \equiv |E_{\text{tot}}|^{1/2} \|\mathbf{L}\| G^{-1} M_{\text{tot}}^{-5/2}$, where E_{tot} is

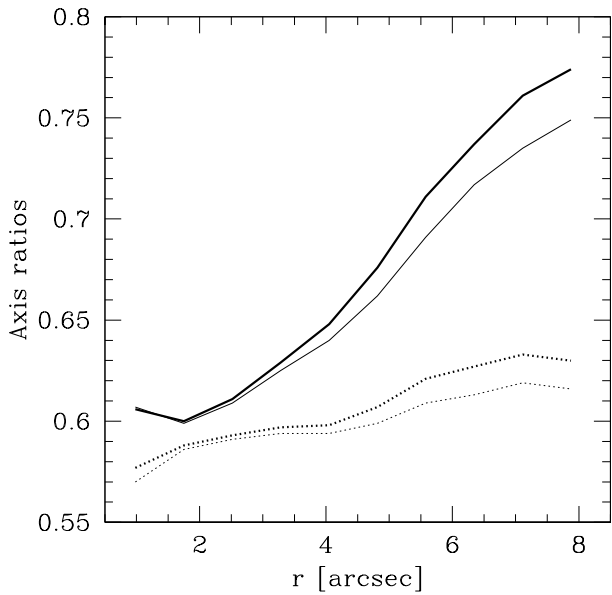


Figure 1. Axis ratios b/a (solid curves) and c/a (dotted curves) as functions of radius for the stellar (thin curves) and total (thick curves) density distributions of the N-body system used as lens (we assumed $r_* = 1.969$ arcsec).

the total energy, and $M_{\text{tot}} \sim 12 M_*$ is the total mass. Of course, the model can be rescaled to represent physical systems of any size and mass by choosing proper values of M_* and r_* .

We define the minor-to-major (c/a) and intermediate-to-major (b/a) axis ratios of the system at a radius r as the corresponding axis ratios of the inertia ellipsoid of particles within an ellipsoid of angle-averaged radius r (for details, see Nipoti, Londrillo & Ciotti 2002). We find that the system is triaxial, with direction of the principal axes and axis ratios depending on radius. Figure 1 shows b/a (solid curve) and c/a (dotted curve) as functions of radius for the stellar (red) and total (black) density distributions within about the half-mass radius of the stellar component (we assumed $r_* = 1.969$ arcsec, see Section 4). Both the stellar and the total distribution are strongly triaxial at $r \gtrsim 5$ arcsec and mildly triaxial (almost prolate) at $r \lesssim 5$ arcsec. The angle-averaged total density and mass profiles of the model are plotted as solid black curves in Figs. 3 and 4, respectively.

4 CONSTRUCTION OF THE OBSERVABLES

In this Section we detail how the simulated observables (or ‘‘mock data’’) are generated from the dark matter and stellar particle distribution taken from the virialized end-product of the N-body simulation described in Section 3.

In order to convert the N-body simulation in a realistic data set with plausible physical characteristics (effective radius, redshift of lens galaxy and source, Einstein radius), we use as a reference the actual lens galaxy SDSS J2321–097, for which both data analysis and joint lensing and dynamics study are presented in C08. Therefore, we will adopt for the noise level and the sampling of the data (i.e. size and binning of the data grids) the corresponding values of SDSS J2321–097.

First, we impose for the simulated galaxy the same redshift of

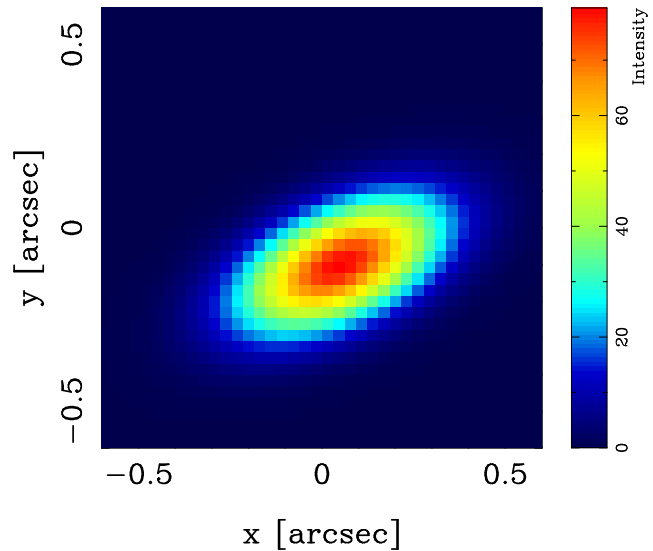


Figure 2. Mock source to be lensed. This is an elliptical Gaussian brightness distribution with $\sigma_x = 0.2$ arcsec, $\sigma_y = 0.1$ arcsec, position angle $\vartheta_{\text{PA}} = 115^\circ$ and with a slight offset with respect to the lens center.

SDSS J2321–097, i.e. $z_l = 0.0819$. The adopted source (Fig. 2) to produce the artificial lensed image is an elliptical Gaussian distribution, slightly offset with respect to the center of mass of the lens galaxy and (again in analogy with SDSS J2321–097) located at a redshift $z_s = 0.5342$. We then fix the values $r_* = 3$ kpc ($\simeq 1.969$ arcsec at redshift z_l) and $M_* = 3 \times 10^{11} M_\odot$ for, respectively, the length and mass units of the simulated galaxy. This setup produces a galaxy that, when is observed along an arbitrary line of sight, displays realistic values for both the effective radius R_e (~ 5 – 6 arcsec, corresponding to ~ 8 kpc at the redshift z_l), and for the Einstein radius R_{Einst} (~ 2 arcsec).

With this choice of r_* and M_* , the simulated galaxy is a massive system of total mass $3.6 \times 10^{12} M_\odot$, with a dark halo which extends up to several hundred kpc. In analogy with the data set of SDSS J2321–097, the spatial coverage of our data is confined to the very inner regions of the galaxy, approximately corresponding to $R_e/2$. However, a fair amount of information comes also from more distant regions of the system which are seen in projection along the line-of-sight (see discussion in C08).

We define for the galaxy an orthogonal reference frame with the origin in the center of mass of the simulated system; the z axis is oriented along the direction of the total angular momentum of the stellar component. Since all the observables are quantities projected in the sky plane, we select three orthogonal lines of sight along which the simulated galaxy is assumed to be observed. In this way, from a single simulation, we obtain three different data sets. The first line of sight is chosen to be approximately oriented along the z axis of the galaxy, and therefore in the following we will refer to the corresponding projection as the xy -plane projection or, for simplicity, the ‘‘face-on’’ projection. The remaining two projections are taken along mutually orthogonal axes both perpendicular to the first line of sight and will be called the yz - and zx -plane projections or, for brevity sake, the ‘‘edge-on’’ projections.

The circularized half-light radii for the three projections are found to be $R_e = 5.227$ arcsec (yz -plane), 5.359 arcsec (zx -plane) and 6.156 arcsec (xy -plane).

When considering any one of the three projections, we will always indicate as z' the direction of the particular line-of-sight.

For each projection, the observables are then calculated following the same procedure:

(i) *Lensed image.* All the particles (both stellar and dark matter ones), properly weighted by the respective masses, are cast in projection along the line-of-sight and binned in a 2D-grid along the sky plane in order to generate from the total density ρ_{tot} a projected density map Σ_{tot} . The latter, once normalized to the critical density $\Sigma_{\text{cr}} = (c^2/4\pi G)(D_s/D_d D_{ds})$, a quantity which depends only on geometry of the system⁴, yields the convergence field κ on the projection plane. The two-dimensional Poisson equation $\nabla^2\psi = 2\kappa$ relates the convergence to the projected potential ψ , whose gradient immediately gives the deflection angle vector field: $\alpha = \nabla\psi$ (see e.g. Schneider, Ehlers & Falco 1992).

We make use of a square grid of 3000×3000 bins for the convergence. The grid size (equivalent to ~ 40 arcsec) is such that it contains, in projection, about half of the total number of particles. Including more distant particles does not have any discernible effect on the outcome, except slowing down all the related calculations, since the number of bins must be increased in order to keep the resolution constant. The Poisson equation is then solved via fast Fourier transform, using the freely available package FFTW (Frigo & Johnson 2005), and enabling us to obtain, from the convergence (appropriately padded in order to avoid numerical issues with the Fourier transform), the two components of deflection angle α . With these deflection angle maps and the mock source described above, the CAULDRON code can straightforwardly generate the lensed image, already convolved with the HST/ACS F814W point spread function (PSF) obtained with TINY TIM (Krist 1993). The lensed image is constructed (in analogy with the lensing data for SDSS J2321–097) on 100×100 grid, with each pixel corresponding to 0.05 arcsec. Finally, a noise distribution based on the covariance maps of the HST images of SDSS J2321–097 is added to the lensed image map in order to produce the final data set.

The obtained lensing data sets for the three projections are shown in the upper right panel of Figs 5, 7 and 9.

(ii) *Surface brightness distribution.* We assume that the stellar mass-to-light ratio is independent of position. The stellar particles are cast along the chosen line-of-sight on a 2D-grid in the sky plane. Such grid is padded and oversampled by a factor of 3 with respect to the final grid adopted for this observable (see later). This is necessary since, in order to take into account the effect of seeing, we have to convolve this quantity with the PSF (here modelized as a Gaussian distribution of FWHM = 0.10 arcsec). The map is then resampled, generating the surface brightness distribution of the galaxy on a 50×50 grid (1 pixel = 0.10 arcsec). Mock noise is then added consistently with the corresponding variance maps of SDSS J2321–097. These images are to first-order equivalent to HST-NICMOS images.

The obtained data sets for the surface brightness distribution of the three projections are shown in the upper left panel of Figs 6, 8 and 10.

(iii) *Line-of-sight projected velocity moments.* The procedure to generate the kinematic maps is similar to the one described above for the surface brightness distribution, including the oversampling and convolution with the Gaussian PSF (but with a broader FWHM = 0.90 arcsec, typical for ground-based observations with the VLT).

⁴ D_s , D_l and D_{ls} are the angular diameter distances from the observer to the source, from the observer to the lens and from the lens to the source, respectively.

Table 1. Recovered non-linear parameters of the best power-law models for the three data sets (obtained as projection of the simulated systems on the three orthogonal planes indicated in the columns): inclination i (in degrees), shear strength ζ and angle ϑ_ζ (in degrees), lens strength α_0 , logarithmic slope γ' and flattening q .

	yz-plane	zx-plane	xy-plane
i	56.5	88.9	53.6
ζ	5.36×10^{-2}	8.71×10^{-2}	5.99×10^{-2}
ϑ_ζ	-24.6	32.4	27.8
α_0	0.652	0.642	0.520
γ'	2.214	2.078	2.234
q	1.000	1.124	0.864

The only difference is that now the velocities projected along the line-of-sight (v_z and v_z^2 for the two kinematic maps respectively) associated with each particle are summed up on each cell, producing the unweighted maps to be used by CAULDRON. These maps can be divided by the surface brightness distribution sampled on the same grid (the “kinematic” grid) in order to obtain the weighted maps, i.e. the quantities $\langle v_z \rangle$ and $\langle v_z^2 \rangle$. The projected velocity dispersion is obtained as $\sigma_z^2 = \langle v_z^2 \rangle - \langle v_z \rangle^2$.

Due to the challenges of spectroscopic observations of distant early-type galaxies, the kinematic grids of SDSS J2321–097 have only 9×9 elements, with 1 pixel = 0.67 arcsec (i.e. the VLT-VIMOS IFU fiber size). Since we are mimicking those observations, we adopt the same grid. As usual, the mock noise is added according to what we know from SDSS J2321–097.

The obtained kinematic data sets for the three projections are presented in the upper central (for the line-of-sight velocity) and upper right (for the line-of-sight velocity dispersion) panels of Figs 6, 8 and 10.

5 ANALYSIS AND RESULTS

In this section we illustrate the results of the joint lensing and dynamics analysis performed with CAULDRON on the three data sets generated (as described in Section 4) from orthogonal projections of the simulated galaxy.

5.1 Recovered structure

As discussed in Section 2, we have adopted an axisymmetric power-law profile as a model for the total density distribution. The recovered non-linear parameters of the best models for the three data sets are reported in Table 1. The non-linear parameters listed in the Table are the inclination i (in degrees), the shear strength ζ and angle ϑ_ζ (in degrees), the lens strength α_0 , the logarithmic slope γ' and the flattening q (a q larger than 1 denotes a prolate axisymmetric shape). In order to speed up the optimization routine, the best values for the lens center and galaxy position angle were determined via preliminary runs, and afterwards were kept fixed (this procedure is commonly used in this kind of analysis: see e.g. C08). The core radius R_s was initially set free as an additional non-linear parameter, but, in order to make the optimization faster, it was later fixed to a negligibly small value after verifying that the introduction of this new parameter did not lead to an increase of the value of the evidence merit function (and therefore in a Bayesian sense the additional complexity was not justified). The optimization routine

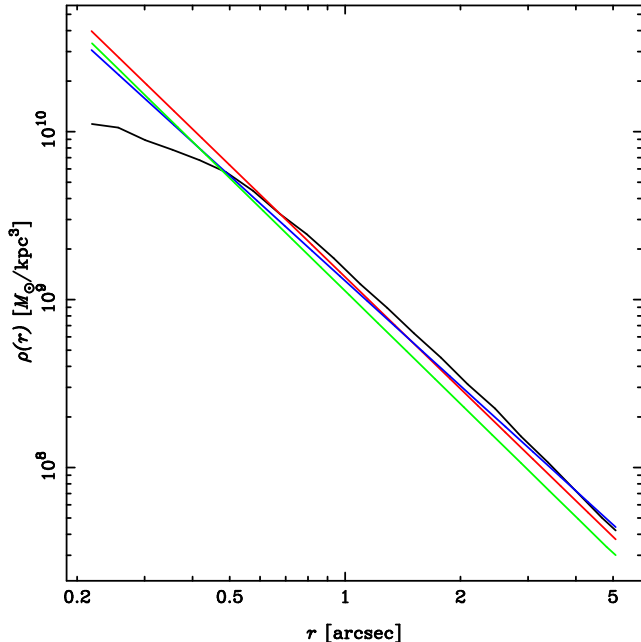


Figure 3. Angle-averaged total density profile of the simulated system (black line) compared with the density profiles of the recovered best models (see Table 1) for the three orthogonal projections data sets. The yz -plane model (red line) has a logarithmic density slope $\gamma'_{yz} = 2.214$, the zx -plane model (blue line) has a slope $\gamma'_{zx} = 2.078$, and the xy -plane model (green line) has a slope $\gamma'_{xy} = 2.234$.

yields also the best value for the three hyperparameters which set the ideal level of regularization.

The reconstructed observables for gravitational lensing and stellar dynamics that correspond to the best model for the yz -plane data set are presented and compared to the data in Figs 5 and 6, respectively. Analogously, Figs. 7-8 and 9-10 show the same quantities for the zx -plane and xy -plane (i.e. face-on projection) data sets.

It is apparent that the residuals of the reconstructed lensed image are fairly large, in particular in the cases of the zx - and xy -plane projections, where moreover the reconstructed source appears patchy and unrealistically pixelized, despite the regularization. The same effects, while less pronounced, are discernible also in the case of the yz -plane projection, where the reconstruction was most successful. This is a clear indication that the underlying total density distribution is actually more complex or inhomogeneous than the simple power-law profile that we are using as a model (see Section 5.3 for a more extended discussion) and that the model is unable to de-lens all lensed images simultaneously into a single well-defined source.

The surface brightness distribution and the kinematics appear to be reasonably well reconstructed. However, in the inner region the reconstructed velocity dispersion is more peaked than in the data, with the possible exception of the zx -plane data set (the one for which the recovered slope is the most shallow, cf. Table 1). Together with the faint central image visible in all the lensing data sets, this indicates that the total density distribution of the system is shallower in the central regions than in the outer regions, as confirmed by the direct analysis of the angle-averaged density profile of the object (see Fig. 3).

Despite several indications from the reconstructed observables that the adopted power-law model is probably oversimplified for

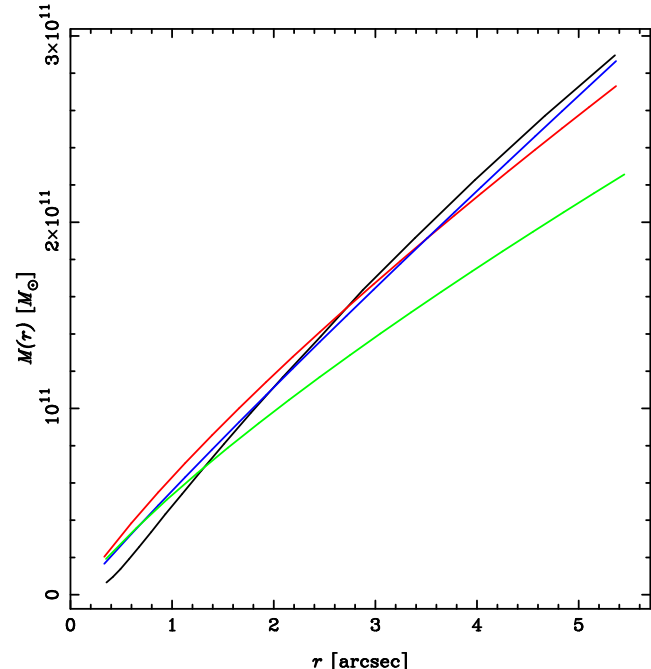


Figure 4. Angle-averaged total mass distribution of the simulated system (black line) compared with the total mass profiles of the recovered best models (see Table 1) for the three orthogonal projections data sets: yz -plane model (red line), zx -plane model (blue line) and xy -plane model (green line).

the data at hand, we find that such a model still provides a satisfactory description of the essential features of the system, and various important physical quantities are robustly recovered.

The angle-averaged total density profiles corresponding to the best models of Table 1 for the three data sets are plotted in Fig. 3 and compared with the true profile of the simulated system. The density slope, which is very close to $\gamma' \sim 2.2$, is quite accurately recovered beyond the inner ~ 0.5 arcsec. The zx -plane model presents a slightly shallower profile ($\gamma' \sim 2.1$), although the discrepancy is small. The xy -plane model, which in general provides the worst recovery of the true quantities (as it will be further discussed in this Section), has a density normalization which is lower than the real one, but manages to catch almost perfectly the correct density slope. In the inner half arcsecond, the density profile of the simulated galaxies becomes shallower ($\rho \sim 1/r$), a feature that the power-law model is obviously unable to capture, although, as already discussed, we have other signals (e.g. from the velocity dispersion) that the model breaks down in that approximate region, and that this is due to the presence of a break in the density profile. Slightly more sophisticated models, such as a double power-law or a single power-law with an added break radius, have also been explored, but the reconstruction of the observables does not improve significantly and the additional complexity is therefore penalized by the Bayesian evidence in favour of the single power-law. In light of what we know from the direct examination of the simulated object, the reason for this failure is that the transition from the $\rho \sim 1/r^2$ region to the $\rho \sim 1/r$ region is too abrupt to be adequately reproduced by these models, and therefore they do not perform significantly better than the simpler single power-law.

Whereas the density slope is a substantially unharmed survivor of the crash test, the recovered flattening and inclination angle are not reliable parameters in case the systems deviate too dras-

Table 2. Dark matter fraction within a sphere of radius $r = R_e$ (first column) and within the line-of-sight oriented cylinder of radius $R = R_e$ (second column) for the three best models. The corresponding quantities for the true system within the same radius are also presented.

	DM fraction (sphere)	DM fraction (cylinder)
<i>yz</i> -plane model ($R_e = 5.''23$)	0.20	0.29
true system (at the same radius)	0.16	0.33
<i>zx</i> -plane model ($R_e = 5.''36$)	0.24	0.37
true system (at the same radius)	0.16	0.34
<i>xy</i> -plane model ($R_e = 6.''16$)	0.19	0.25
true system (at the same radius)	0.20	0.35

tically from the model's assumptions. One should note, however, that these quantities are only properly defined for an axisymmetric object, and therefore do not have a straightforward interpretation when directly applied to a simulated system which is approximately triaxial and whose axis ratios also change as a function of radius (as seen in Section 3). The best models for the *yz*-plane and *xy*-plane data set both give an inclination close to $\sim 55^\circ$, so there is no sign that the latter is interpreted as a face-on system. The *zx*-plane best model, on the other hand, turns out quite correctly to be an almost edge-on system ($i \simeq 90^\circ$). As for the flattening, it appears that the axisymmetric model, faced with the insurmountable problem of triaxiality, tends to adopt a density profile close to spherical (almost exactly spherical in the case of the *yz*-plane data set, slightly prolate or oblate in the cases of the *zx*- and *xy*-plane data sets, respectively).

5.2 Total mass distribution and dark matter fraction

Closely connected to the density profile is the (angle-averaged) total mass distribution, plotted in Fig. 4 for the three best models and the true system. We find that in the case of the edge-on projections models (*yz*- and *zx*-planes) the mass profile is very well reproduced within a few percent. The mass profile of the face-on projection model is instead underestimated of about 25 percent within a sphere of radius ~ 5 arcsec: this is a consequence of the too low density normalization which is recovered for this model, as previously seen in Fig. 3. Because of the tight constraints imposed by the lensing, the total projected mass enclosed within R_{Eins} is within a few percent from the correct value for all three models.

A quantity of extreme interest in the study of early-type galaxies is the dark matter fraction of these objects. It is therefore important to be able to test how reliable is the CAULDRON method in estimating this parameter also for systems that defy its assumptions of axisymmetry and two-integral DF. Since the method only provides a total density distribution, however, it is necessary to make further assumptions to be able to constrain the stellar density profile. In order to limit as much as possible the arbitrariness of such assumptions we adopt, as in the analysis of real galaxies, the so-called “maximum bulge” approach (cf. C08). This consists in maximizing the contribution of the luminous component (which is obtained as an output of the best model reconstruction), i.e. maximally rescaling the stellar density distribution without exceeding the total density distribution, assuming that the stellar mass-to-light ratio is in-

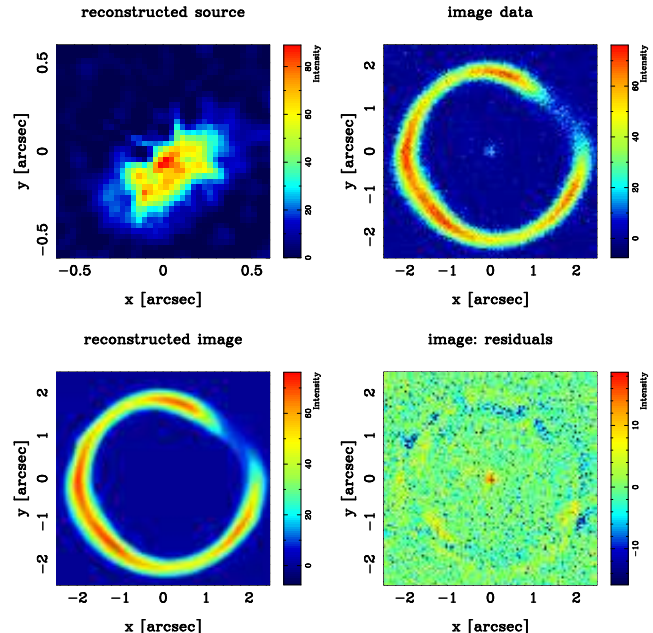


Figure 5. Best model lens image reconstruction for the *yz*-plane data set (the generation of the simulated observables is detailed in Section 3). From the top left-hand to bottom right-hand panel: reconstructed source model; simulated noisy data showing the lensed image; lensed image reconstruction; residuals.

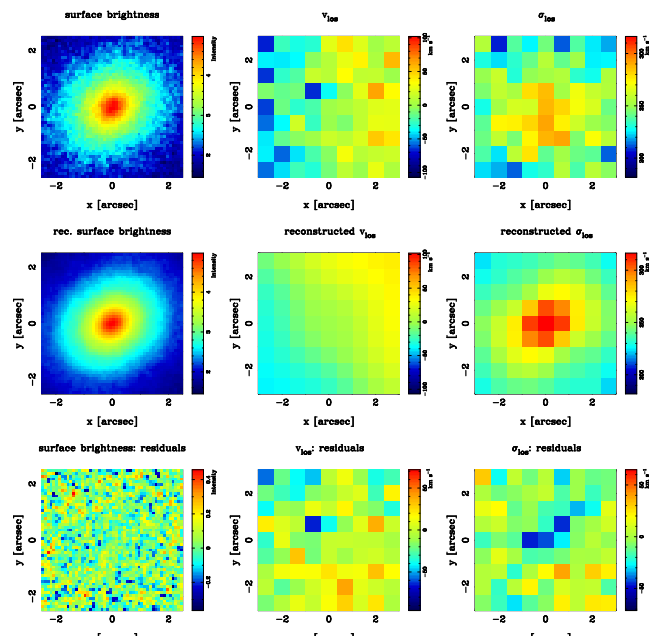
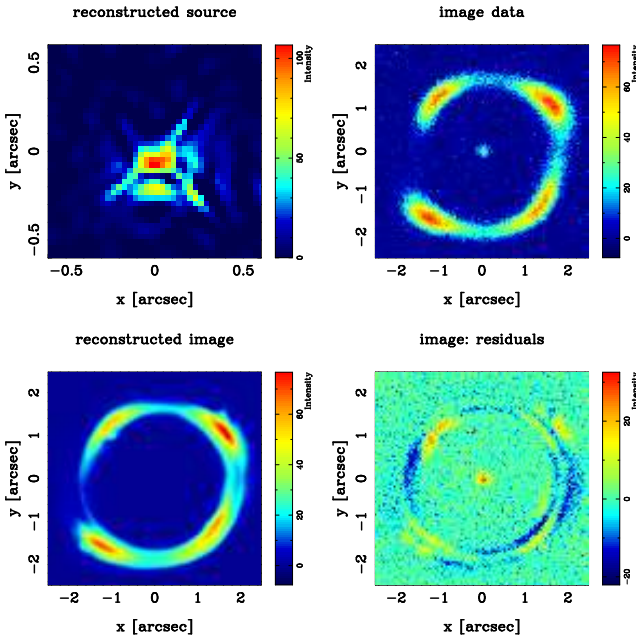
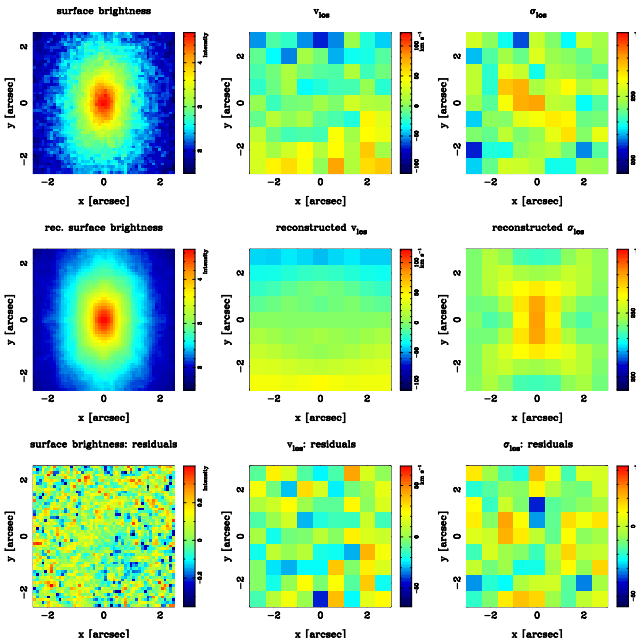


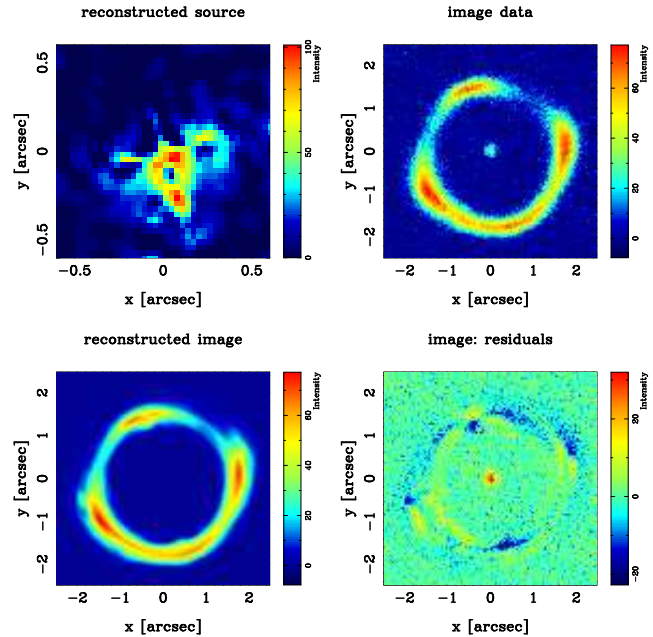
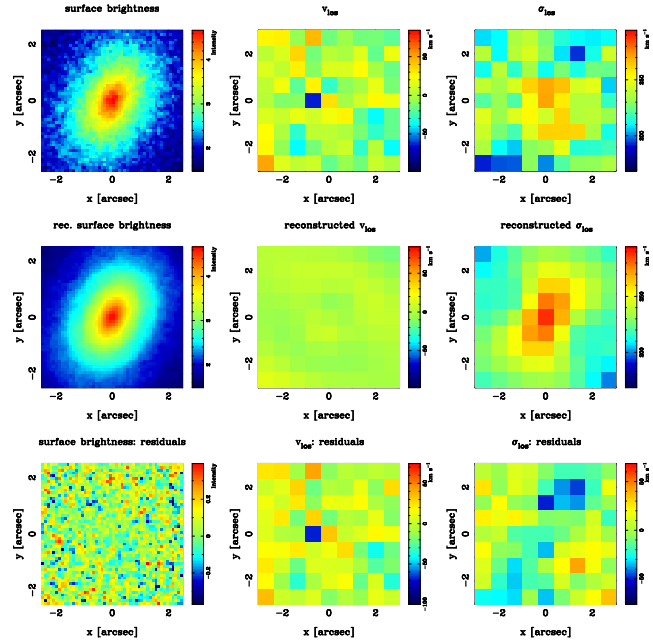
Figure 6. Best dynamical model for the *yz*-plane data set. First row: simulated noisy surface brightness distribution, projected line-of-sight velocity and line-of-sight velocity dispersion. Second row: corresponding reconstructed quantities for the best model. Third row: residuals.

dependent of position. This method gives a lower limit for the dark matter fraction, provided that the model's assumptions hold true.

Under the maximum bulge hypothesis, we study both the volume mass ratio (i.e. the dark matter fraction within a sphere of radius taken to be equal to the effective radius of the considered data set) and the projected mass ratio (i.e. the dark matter fraction within

Figure 7. Same as Fig. 5, but relative to the zx -plane data set.Figure 8. Same as Fig. 6, but relative to the zx -plane data set.

a cylinder oriented along the line-of-sight with a radius equal to R_e). The results of this analysis for the three best models are summarized in Table 2, which also shows the corresponding quantities for the true system (at the appropriate radii). We find that the dark matter fraction is remarkably well recovered for all three models, and it is within 10% (in total mass) of the correct value for both the volume and the projected mass ratio. The largest discrepancy (10% within the cylinder) is found for the face-on model, as usual the most problematic one, while the yz -plane model (which is the one that best reproduces the observables, in particular the lensed image) manages to accurately recover the dark matter fraction within $\lesssim 5\%$ of the correct value.

Figure 9. Same as Fig. 5, but relative to the xy -plane data set.Figure 10. Same as Fig. 6, but relative to the xy -plane data set.

It must be noted that we assumed a position-independent stellar mass-to-light ratio both in constructing the surface-brightness map from the N-body system and in estimating the maximum stellar mass for the best-fit models. In real galaxies the stellar mass-to-light ratio might depend on position, though the effect of a non-uniform stellar mass-to-light ratio is not expected to be strong based on observed colour gradients (e.g. Kronawitter et al. 2000).

5.3 Reconstructed source

As it can be immediately seen by an examination of Figs 5, 7 and 9, the lensed image reconstruction for the three models is far from the

noise level, and the reconstructed source – with the partial exception of the yz -plane model – has little in common with the simulated source (Fig. 2) used to generate the lensed images. Even assuming that one has no information about the actual source (as it would be the case for real data sets) it is evident that the reconstructed sources are unrealistically irregular and pixelized. We remark that this is a consequence of having an underlying density distribution for the system which is more complex and less homogeneous than the assumed power-law density model. As the present test neatly displays, gravitational lensing is very sensitive to the features of the potential within the Einstein radius, and even small inhomogeneities and departures from the assumed model will generally have a detectable effect⁵. Significantly, such large residuals have never been encountered so far when analysing real lens galaxies, with all the examined SLACS lenses being accurately reconstructed by means of single power-law models, possibly with the inclusion of external shear (Koopmans et al. 2006, Czoske et al. 2008, Barnabè et al., in preparation). This strengthens the statement that the simulated system under analysis, while not being utterly unrealistic, constitutes an extreme case and is therefore well suited for the “crash test” of the code that we aim to conduct. It should be emphasized that, if these were real data sets, from the mere visual inspection of the results of the best lensed image reconstruction provided by CAULDRON, we would already be able to conclude that we are dealing with a unusually complex galaxy, which would surely deserve a more sophisticated modelling once the preliminary study is completed.

In order to better understand the limitations of the axisymmetric approach and the cause for the large residuals in the reconstructed image, the same data set (i.e. yz -plane projection) has been analysed by means of the adaptive Bayesian strong lensing code of VK08, which can account for small corrections in the projected potential, and therefore for departures from symmetry and for the presence of clumpiness and substructure in the convergence, but which does not include any constraint from the dynamics. Starting from the best model axisymmetric potential of Table 1 and then introducing small potential corrections and letting the parameters vary, it is found that the lensed image can be reconstructed down to the noise level, and the source is quite accurately recovered, by making use of an adaptive grid, as shown in Fig. 11. As it is visible in the convergence map of Fig. 11 (bottom-right panel), there are two main overdensities (with respect to the best model density profile), located on opposite sides with respect to the center. These overdensities are at least an order of magnitude too weak to be indicative of the presence of a genuine localized massive dishomogeneity in the simulated system (cf. VK08 and in particular their Figs. 8 and 9), which is rather smooth and does not present massive substructures. These features in the convergence map are therefore due, rather than to clumpiness, to the deviation of the true (projected) mass distribution from the simple assumption of elliptical shape.

5.4 Recovered dynamical quantities

A reliable knowledge of the dynamical structure of early-type galaxies would constitute a valuable asset for all the formation and

⁵ As a consequence, gravitational lensing can actually be used to quantify the level of mass substructure in massive galaxies, through their effect on highly-magnified arcs and Einstein rings (see e.g. Vegetti & Koopmans 2008, hereafter VK08).

Table 3. Recovered dynamical quantities for the three best models (last three columns) compared with the true values directly calculated from the N-body system (second column). The dynamical quantities are L_z (in units of kpc km s^{-1}), the V/σ ratio, and the three global anisotropy parameters δ , β and γ . See text for a more exhaustive description.

	true value	yz -plane	zx -plane	xy -plane
L_z	-143.1	-142.6	-143.3	16.8
V/σ	0.170	0.152	0.214	0.130
β	0.301	$\equiv 0$	$\equiv 0$	$\equiv 0$
γ	0.208	-0.470	-0.645	-0.986
δ	0.219	0.190	0.244	0.330

evolution models. Therefore, in this Section we investigate how accurately the axisymmetric CAULDRON code can recover the essential dynamical characteristics of the simulated system. We expect comparable performances (and typically better ones) when the code is applied to real galaxies.

Since the dynamical modelling block of CAULDRON (see Section 2) does not employ an actual orbit-superposition method, a detailed analysis of the orbital families of the galaxy is beyond reach. However, we are able to study fundamental global dynamical quantities such as angular momentum, V/σ and anisotropy parameters. The results of this study for the three models, compared with the true quantities calculated directly from the simulated system, are listed in Table 3.

The total angular momentum along the principal rotation axis, L_z , has been calculated for the three models and the simulated system within the same cylindrical region of radius $R = 5''$ and height $z = 5''$ (this is a square box in the meridional plane, of linear size comparable to the effective radius; all the dynamical quantities have been calculated within this region). As seen in Table 3, L_z is accurately recovered for the two edge-on projection models, with discrepancies of less than 10% from the correct value, despite the fact that the line-of-sight velocity maps are considerably noisy⁶. On the contrary, in the case of the face-on projection model, where little or no information about the rotation is available from the kinematic data (see top-middle panel of Fig. 10: the map displays essentially no rotation) the recovered L_z is obviously incorrect, being of the opposite sign and, more importantly, quite close to zero. This clearly highlights the great importance of the information enclosed in the kinematic maps, despite the fact that such maps are usually much more noisy and considerably more coarsely sampled, in terms of number of pixels, than the surface brightness or lensed image maps. On the opposite side, this result also cautions us in being aware of the possible shortfalls of the method when studying galaxies whose data show no discernible rotation.

The global quantity V/σ (see Binney 2005; Cappellari et al. 2007) is an indicator of the importance of rotation with respect to the random motion. We find here that a value not too far from the correct one is recovered for the edge-on projection models, although the discrepancies are larger than in the case of the angular momentum (the difference is of order 10% for the yz -plane model

⁶ The mock galaxy displays also some rotation along the orthogonal axes, although the angular momentum along these directions is only of order $\lesssim 1\%$ of L_z . Because of its intrinsic properties, the model is not capable of reproducing this kind of rotation (in other words, L_x and L_y are always 0 by construction).

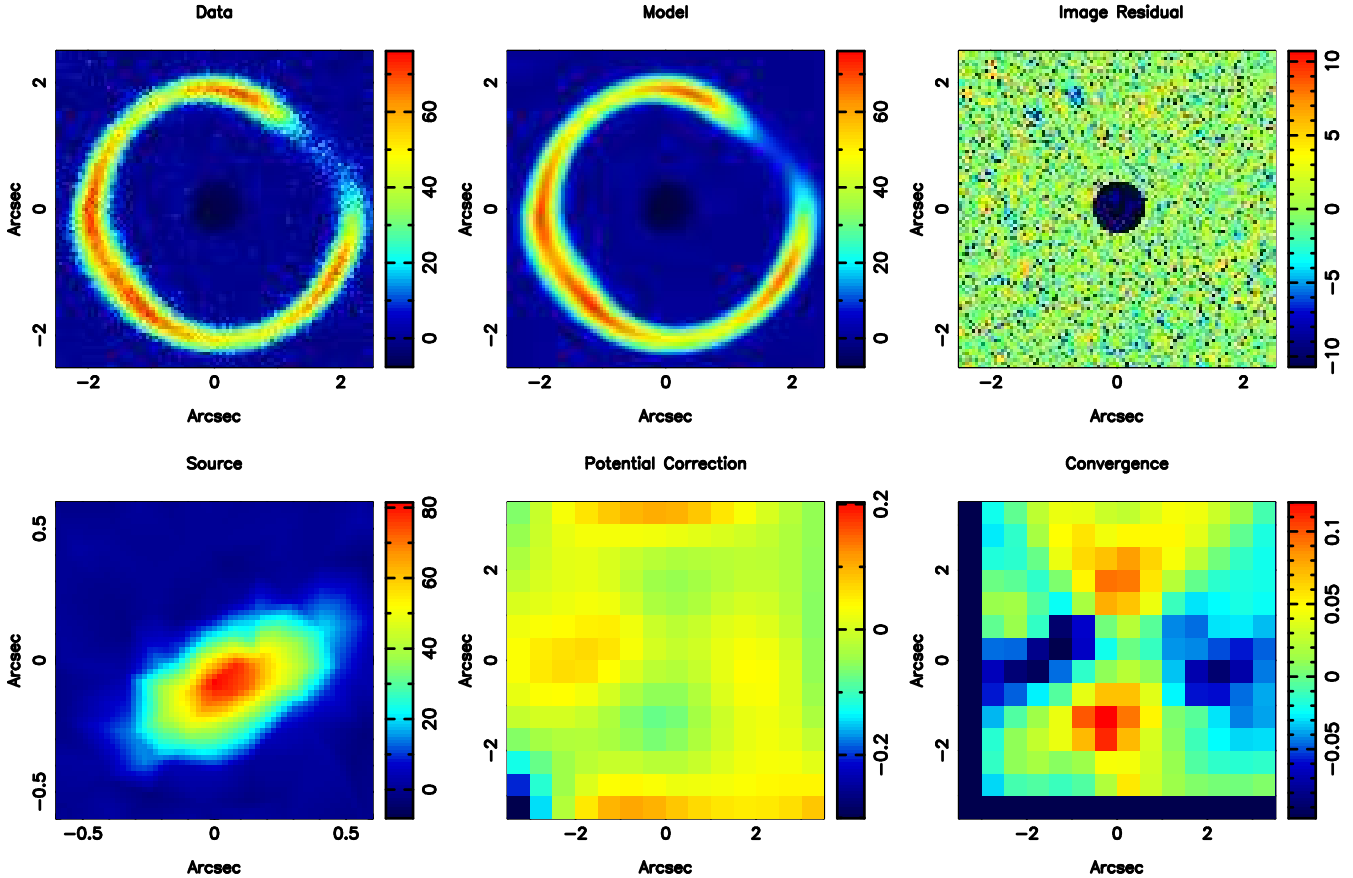


Figure 11. Result of the linear source and potential reconstruction for the yz -plane dataset, as obtained by applying the adaptive Bayesian lensing code of VK08. The first row shows, from left to right, the lensed image data set, the reconstructed image and best source. The second row presents, from left to right, the image residuals, the total potential correction and the substructure convergence.

and 25% for the zx -plane model), and even the face-on projection model, while underestimating the importance of rotation of about 25%, gives a quite reasonable result.

The anisotropy distribution is another very relevant dynamical quantity, often considered an important indicator of the galaxy formation processes. Since the simulated system is severely non-spherical, however, the anisotropy profile cannot be reliably described and compared to the models by making use of a simple radial parameter such as the commonly used $\beta_r(r) \equiv 1 - \sigma_{\tan}^2(r)/\sigma_{\text{rad}}^2(r)$, where σ_{\tan} and σ_{rad} are the tangential and radial velocity dispersions, respectively. Instead, a more robust and consistent indicator is provided by the three global anisotropy parameters defined in Cappellari et al. (2007) and Binney & Tremaine (2008):

$$\beta \equiv 1 - \frac{\Pi_{zz}}{\Pi_{RR}}, \quad (6)$$

$$\gamma \equiv 1 - \frac{\Pi_{\varphi\varphi}}{\Pi_{RR}}, \quad (7)$$

$$\delta \equiv 1 - \frac{2\Pi_{zz}}{\Pi_{RR} + \Pi_{\varphi\varphi}} = \frac{2\beta - \gamma}{2 - \gamma}, \quad (8)$$

where

$$\Pi_{kk} = \int \rho \sigma_k^2 d^3x \quad (9)$$

and σ_k denotes the velocity dispersion along the direction k at any given location in the galaxy. For a two-integral DF $\sigma_R^2 = \sigma_z^2$ every-

where, which implies $\Pi_{RR} = \Pi_{zz}$, so that the value of β is always zero. Therefore, due to the simplifying assumptions on the distribution function, our method will generally fail in recovering the true β value when analysing a more complex system. We clearly observe this in the present study, where $\beta = 0.301$ for the simulated system (see again Table 3). Not too unexpectedly, since the global anisotropy parameters are related, this has disrupting consequences also on the recovered γ , which is always negative, indicating mild tangential anisotropy in the models, while the mildly radially anisotropic N-body system has a positive γ . This discrepancy is confirmed by inspecting the radial behaviour of a kinetic energy proxy for $\beta_r(r)$, i.e. the quantity $\beta_K(r) \equiv 1 - K_{\tan}(r)/K_{\text{rad}}(r)$, where K_{\tan} and K_{rad} are, respectively, the spherically-averaged tangential and radial components of the kinetic energy. Interestingly, however, the global parameter δ is remarkably robust, particularly for the two edge-on projection models, with a discrepancy of order $\sim 15\%$ from the true value.

5.5 Uncertainties

In this section we present the statistical uncertainties on the model parameters calculated by making use of the identical procedure which is used when dealing with real systems.

Bayesian statistics represents a powerful tool for data analysis, model comparison and model parameters constraining. A major improvement in this direction has been made with the introduction of

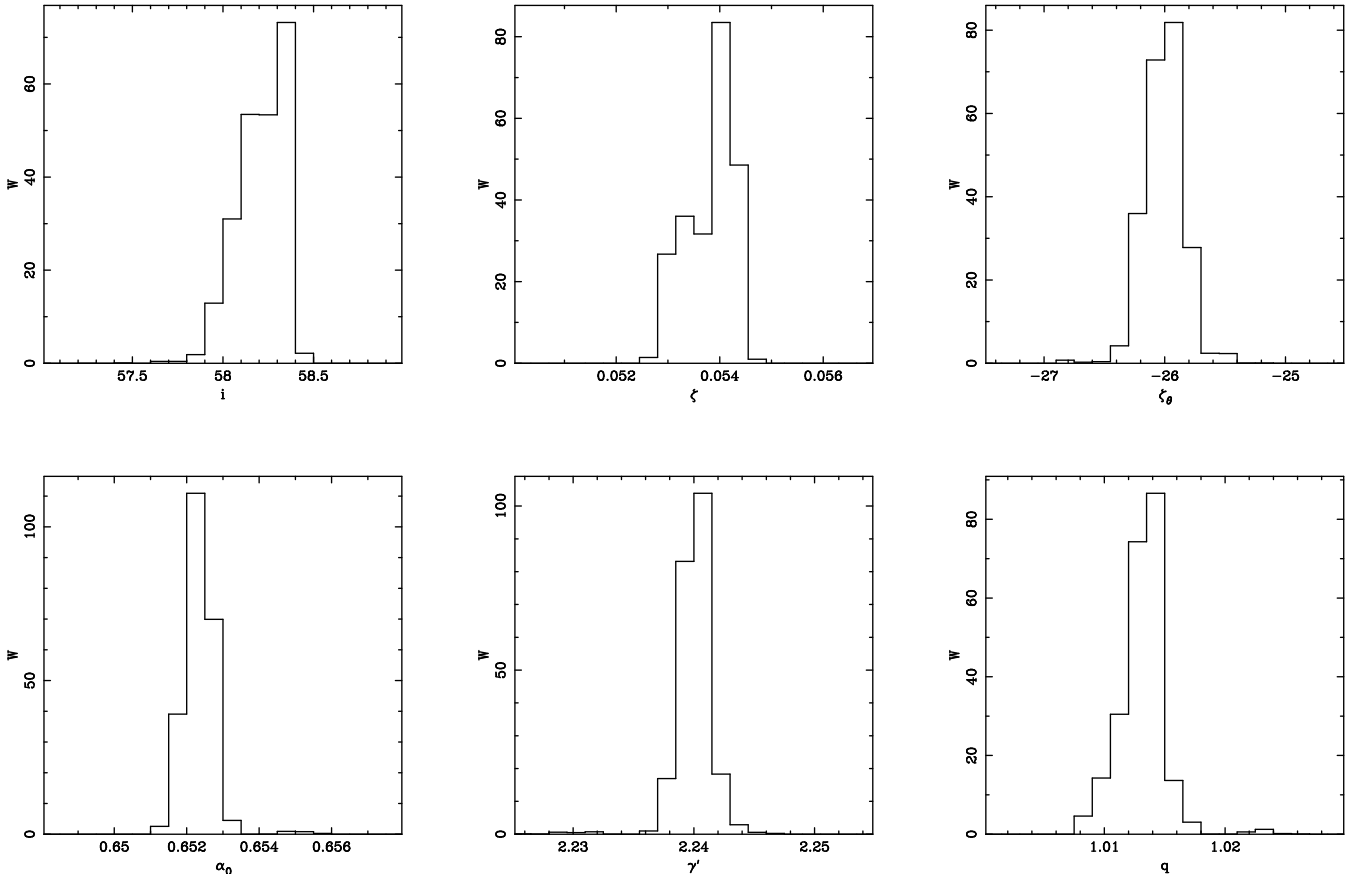


Figure 12. Posterior probability distribution for the non-linear parameters of the best power-law model for the yz -plane projection data set, as obtained from the Nested Sampling evidence exploration. The width of the posterior probability distribution has been calculated for each of the parameters, by considering the region around the peak which contains 99% of the probability, yielding: $i = [57.81, 58.45]$, $\zeta = [0.05273, 0.05455]$, $\vartheta_\zeta = [-26.55, -25.47]$, $\alpha_0 = [0.6512, 0.6550]$, $\gamma' = [2.231, 2.244]$, $q = [1.008, 1.023]$.

the Nested Sampling technique developed by Skilling (2004) (see also Sivia & Skilling 2006 and e.g. Mukherjee, Parkinson & Liddle 2006 for an astrophysical application). This method provides a computationally efficient way to calculate the total marginalised evidence, which is the key quantity for model comparison, and in addition yields other valuable information, such as the posterior probability density distributions, the mean values and the standard deviations for each of the model parameters. The Nested Sampling technique has been applied in the context of lensing and model-comparison by VK08.

Bayesian statistics requires to formalize one's assumptions by defining priors P on the parameters η_i (see e.g. Mackay 1992). We choose the priors to be uniform in a symmetric interval of size $\delta\eta_i$ around the best recovered values $\eta_{b,i}$, that is:

$$P(\eta_i) = \begin{cases} \text{constant} & \text{for } |\eta_{b,i} - \eta_i| \leq \delta\eta_i \\ 0 & \text{for } |\eta_{b,i} - \eta_i| > \delta\eta_i \end{cases} \quad (10)$$

In order to make sure that the priors include the bulk of the evidence likelihood, very conservative estimates of the intervals $\delta\eta_i$ are obtained by means of fast preliminary runs.

The posterior probability distributions (PPDs) for each parameter obtained from the Nested Sampling analysis are shown in Fig. 12 for one of the models (yz -plane projection). Within the context of Bayesian statistics, each PPD histogram quantifies the error for the considered parameter given the data and all the assumptions

(i.e. under the hypothesis that the adopted model is the correct one); since the many pixels in the data sets provide a lot of constraints, these errors are typically very small, as is the case in the plot presented here. It should be noted that, because of the marginalization over all the parameters except the one under analysis, the PPD usually provides the most conservative estimate of statistical errors. At the same time, however, due to projection effect arising from the marginalization itself, the mean value of the parameter obtained from the PPD can be significantly skewed with respect to the best recovered value of the corresponding parameter obtained from the best model (P. Marshall, private communication).

However, the statistical errors cannot take into account or give an estimate of the systematic uncertainties, which are frequently much larger than the former. In our case, significant systematic errors arise mostly due to the adoption of an oversimplified model⁷. The entity of the systematic uncertainties can be quantified, at least as a first order approximation, by looking at the discrepancies between the recovered parameters for the three data sets best models.

⁷ In real datasets of lens galaxies, sources of systematic errors which raise particular concern are, for example, the PSF and the subtraction of the lens galaxy surface brightness (see e.g. the detailed study of Marshall et al. 2007).

6 DISCUSSION AND CONCLUSIONS

We have applied **CAULDRON**, currently the most advanced code for joint gravitational lensing and stellar dynamics analysis of early-type galaxies, to a galaxy model with dark matter halo resulting from a numerical N-body simulation of galaxy merging. Such a N-body system, which we use as lens, significantly violates the two major assumptions upon which the algorithm is based, namely axial symmetry of the total density distribution and two-integral stellar distribution function. The purpose of this crash test is to investigate how the code will perform or fail in an extreme case, and to identify the quantities which can still be reliably recovered. Such robust quantities are expected to be recovered with at least comparable accuracy when **CAULDRON** is employed in the analysis of real galaxies which, while not necessarily axisymmetric or described by a two- (or three-) integral DF, will hardly depart from the code's assumptions more severely than the simulated system studied here.

Further complications can also arise, in general, due to the effects of the environment on the lens galaxy. However, the SLACS galaxies, despite living in overdense regions as expected for massive early-type galaxies, are not found to be significantly affected by the contribution of the environment or of line-of-sight contaminants (see the in-depth study of Treu et al. 2008). Therefore, since the environment does not play a major role for lens galaxies at least in the redshift range $z \sim 0.1 - 0.4$, we have not considered this issue further in the present paper.

From the N-body system we have generated three data sets corresponding to three orthogonal lines of sight, one of which has been chosen to be approximately oriented along the total angular momentum of the system, in order to obtain a “face-on” projection data set with little or no rotation discernible in the kinematic maps. An elliptical Gaussian surface brightness distribution has been constructed and then gravitationally lensed by the mock galaxy in order to create the lensing data set. We have also taken into account the effect of the PSF and added realistic noise to the simulated data, using as a reference the real data set for the SLACS lens galaxy SDSS J2321–097 studied in C08.

These data sets have been analysed with **CAULDRON**, assuming as a model an axisymmetric power-law total density distribution, with the identical procedure followed in the study of real lens galaxies. In the three cases, the recovered best models, obtained via maximization of the Bayesian evidence, show clear difficulties in reconstructing the observables (in particular the lensed image and the velocity dispersion map) up to the noise level. This is a consequence of having adopted a very simple model which cannot account for the complexity and the lack of symmetry of the true density distribution.

However, the method is still capable of recovering with remarkable accuracy several global structural and dynamical characteristics of the examined system, provided that some information about the galaxy rotation is available from the kinematic maps. In particular:

(i) The logarithmic slope γ' of the total density distribution is a robust quantity which is recovered with remarkable accuracy (within less than 10%), even in the case of the face-on projection data set. While a power-law model cannot account for a break in the actual density profile, indications of its presence will show up in the observables as features which are not reproduced by the best model (e.g. a much flatter central velocity dispersion).

(ii) The angle-averaged total density and total mass radial profiles for the edge-on projection best models are found to closely follow the corresponding true distributions, within approximately

an effective radius. Discrepancies are larger for the face-on projection case.

(iii) The best reconstructed inclination angle and flattening of the total density distribution have little or no relation with the corresponding quantities of the N-body system. We conclude that when the axisymmetric model is applied to a system with a more complex geometry, one can not expect to recover reliable information about its shape.

(iv) By adopting the maximum bulge approach (i.e. maximizing the contribution of the luminous component, assuming a position-independent stellar mass-to-light ratio), it is possible to estimate within approximately 10% (in total mass) the dark matter fraction of the analysed system, whether the mass ratio is calculated within a sphere or within a line-of-sight oriented cylinder of radius $\simeq R_e$.

(v) When rotation is present in the kinematic maps, global quantities such as the angular momentum L_z and the ratio V/σ (a measure of ordered vs chaotic motions) recovered from the best model describe quite reliably (i.e. within $\sim 10\%$ and 25%, respectively) the dynamical properties of the system under analysis. The global anisotropy parameters β and γ are not correctly estimated, i.e. the anisotropy distribution is not robustly recovered by the method unless the analyzed system effectively respects the assumptions of axisymmetry and two-integral distribution function. The anisotropy parameter δ , on the contrary, is found to be a robust quantity even when such assumptions are violated: we recover the correct value within $\lesssim 15\%$ for the edge-on projection data sets.

The major conclusion of our study is that the joint lensing and dynamics code **CAULDRON** can be effectively applied also to the analysis of galaxies which deviate from the (quite restrictive) assumptions of axial symmetry and two-integral stellar DF. This result is very relevant for the analysis of galaxies at $z \gtrsim 0.1$ for which, due to the data limitations, the more powerful methods available at lower redshifts are not viable techniques. Several fundamental structural and dynamical quantities, in particular the total density slope and the dark matter fraction within the region where the data are available, can be recovered with good accuracy. Other quantities, such as L_z and the anisotropy parameter δ , can be reliably recovered provided that rotation is detected in the kinematic maps: when this is not the case (either because of intrinsic properties of the galaxy or because the system is observed face-on) the constraints are much looser and one needs to be very sceptical about the outcomes of the best model relative to these quantities. We point out that special care should be taken when the best model does not manage to reproduce the observables satisfactorily (i.e. at or close to the noise level), in particular the lensed image. This is a strong indication that the true density distribution deviates significantly from the assumptions of the adopted model family, and therefore, while there are still reliable recovered parameters (as listed above), more delicate quantities such as flattening and inclination angle, as well as the reconstructed source, should not be trusted. In these cases, the **CAULDRON** code can provide a robust but only quite general description of the structure of the galaxy, paving the way for the more sophisticated modelling techniques which are necessary (together, if possible, with a better data set) to achieve a deeper and more detailed knowledge of the system.

Interestingly, large residuals in the lensed images reconstruction such as the ones found in this study have never been encountered so far in the analysis of the SLACS sample of lens galaxies (Koopmans et al. 2006, C08) indicating that an axisymmetric single power-law total density distribution constitutes a satisfactory model for these systems.

ACKNOWLEDGMENTS

M. B. acknowledges the support from an NWO program subsidy (project number 614.000.417). L. V. E. K. and S. V. are supported (in part) through an NWO-VIDI program subsidy (project number 639.042.505). M. B. and S. V. are grateful to Phil Marshall for useful discussion.

REFERENCES

Arnaboldi M., Freeman K. C., Mendez R. H., Cappaccioli M., Ciardullo R., Ford H., Gerhard O., Hui X., Jacoby G. H., Kudritzki R. P., Quinn P. J., 1996, *ApJ*, 472, 145

Barnabè M., Koopmans L. V. E., 2007, *ApJ*, 666, 726

Barnes J. E., 1992, *ApJ*, 393, 484

Bertin G., 2000, *Dynamics of Galaxies*. Cambridge University Press

Bertin G., Bertola F., Buson L. M., Danziger I. J., Dejonghe H., Sadler E. M., Saglia R. P., de Zeeuw P. T., Zeilinger W. W., 1994, *A&A*, 292, 381

Binney J., 2005, *MNRAS*, 363, 937

Binney J., Tremaine S., 2008, *Galactic Dynamics*. Princeton University Press

Bolton A. S., Burles S., Koopmans L. V. E., Treu T., Moustakas L. A., 2006, *ApJ*, 638, 703

Borriello A., Salucci P., Danese L., 2003, *MNRAS*, 341, 1109

Cappellari M., Bacon R., Bureau M., Damen M. C., Davies R. L., de Zeeuw P. T., Emsellem E., Falcón-Barroso J., Krajnović D., Kuntschner H., McDermid R. M., Peletier R. F., Sarzi M., van den Bosch R. C. E., van de Ven G., 2006, *MNRAS*, 366, 1126

Cappellari M., Emsellem E., Bacon R., Bureau M., Davies R. L., de Zeeuw P. T., Falcón-Barroso J., Krajnović D., Kuntschner H., McDermid R. M., Peletier R. F., Sarzi M., van den Bosch R. C. E., van de Ven G., 2007, *MNRAS*, 379, 418

Carollo C. M., de Zeeuw P. T., van der Marel R. P., Danziger I. J., Qian E. E., 1995, *ApJ*, 441, L25

Chandrasekhar S., 1969, *Ellipsoidal Figures of Equilibrium*. Yale University Press

Ciotti L., Pellegrini S., 2008, *MNRAS*, 387, 902

Cole S., Lacey C. G., Baugh C. M., Frenk C. S., 2000, *MNRAS*, 319, 168

Cretton N., de Zeeuw P. T., van der Marel R. P., Rix H.-W., 1999, *ApJS*, 124, 383

Czoske O., Barnabè M., Koopmans L. V. E., Treu T., Bolton A. S., 2008, *MNRAS*, 384, 987

de Zeeuw P. T., Bureau M., Emsellem E., Bacon R., Carollo C. M., Copin Y., Davies R. L., Kuntschner H., Miller B. W., Monnet G., Peletier R. F., Verolme E. K., 2002, *MNRAS*, 329, 513

Emsellem E., Cappellari M., Peletier R. F., McDermid R. M., Bacon R., Bureau M., Copin Y., Davies R. L., Krajnović D., Kuntschner H., Miller B. W., de Zeeuw P. T., 2004, *MNRAS*, 352, 721

Evans N. W., 1994, *MNRAS*, 267, 333

Fabbiano G., 1989, *ARAA*, 27, 87

Forbes D. A., Lasky P., Graham A. W., Spitler L., 2008, *MNRAS*, 389, 1924

Franx M., van Gorkom J. H., de Zeeuw T., 1994, *ApJ*, 436, 642

Frigo M., Johnson S. G., 2005, *Proceedings of the IEEE*, 93, 216

Gerhard O., Kronawitter A., Saglia R. P., Bender R., 2001, *AJ*, 121, 1936

Gerhard O. E., 1993, *MNRAS*, 265, 213

Humphrey P. J., Buote D. A., Gastaldello F., Zappacosta L., Bullock J. S., Brighenti F., Mathews W. G., 2006, *ApJ*, 646, 899

Jesseit R., Naab T., Peletier R. F., Burkert A., 2007, *MNRAS*, 376, 997

Koopmans L., Treu T., Bolton A. S., Burles S., Moustakas L. A., 2006, *ApJ*, 649, 599

Koopmans L. V. E., Treu T., 2002, *ApJ*, 568, L5

Krist J., 1993, in Hanisch R. J., Brissenden R. J. V., Barnes J., eds, *Astronomical Data Analysis Software and Systems II* Vol. 52 of *Astronomical Society of the Pacific Conference Series*, Tiny tim : an hst psf simulator. p. 536

Kronawitter A., Saglia R. P., Gerhard O., Bender R., 2000, *A&AS*, 144, 53

Loewenstein M., White III R. E., 1999, *ApJ*, 518, 50

Londrillo P., Nipoti C., Ciotti L., 2003, *Memorie della Società Astronomica Italiana Supplement*, 1, 18

Mackay D. J. C., 1992, *PhD Thesis*

Mackay D. J. C., 1999, *Neural Comp*, 11, 1035

Mackay D. J. C., 2003, *Information Theory, Inference and Learning Algorithms*. Cambridge University Press

Marshall P. J., Treu T., Melbourne J., Gavazzi R., Bundy K., Ammons S. M., Bolton A. S., Burles S., Larkin J. E., Le Mignant D., Koo D. C., Koopmans L. V. E., Max C. E., Moustakas L. A., Steinbring E., Wright S. A., 2007, *ApJ*, 671, 1196

Matsushita K., Makishima K., Ikebe Y., Rokutanda E., Yamasaki N., Ohashi T., 1998, *ApJ*, 499, L13

McDermid R. M., Emsellem E., Shapiro K. L., Bacon R., Bureau M., Cappellari M., Davies R. L., de Zeeuw T., Falcón-Barroso J., Krajnović D., Kuntschner H., Peletier R. F., Sarzi M., 2006, *MNRAS*, 373, 906

Meneghetti M., Bartelmann M., Jenkins A., Frenk C., 2007, *MNRAS*, 381, 171

Mould J. R., Oke J. B., de Zeeuw P. T., Nemec J. M., 1990, *AJ*, 99, 1823

Mukherjee P., Parkinson D., Liddle A. R., 2006, *ApJ*, 638, L51

Nipoti C., Londrillo P., Ciotti L., 2002, *MNRAS*, 332, 901

Nipoti C., Londrillo P., Ciotti L., 2003, *MNRAS*, 342, 501

Nipoti C., Londrillo P., Ciotti L., 2007, *MNRAS*, 381, L104

Pellegrini S., Ciotti L., 2006, *MNRAS*, 370, 1797

Rix H.-W., de Zeeuw P. T., Cretton N., van der Marel R. P., Carollo C. M., 1997, *ApJ*, 488, 702

Robertson B., Cox T. J., Hernquist L., Franx M., Hopkins P. F., Martini P., Springel V., 2006, *ApJ*, 641, 21

Romanowsky A. J., Douglas N. G., Arnaboldi M., Kuijken K., Merrifield M. R., Napolitano N. R., Capaccioli M., Freeman K. C., 2003, *Science*, 301, 1696

Saglia R. P., Bertin G., Stiavelli M., 1992, *ApJ*, 384, 433

Schneider P., Ehlers J., Falco E. E., 1992, *Gravitational Lenses*. Berlin, Springer-Verlag

Schwarzchild M., 1979, *ApJ*, 232, 236

Sivia D. S., Skilling J., 2006, *Data Analysis: A Bayesian Tutorial*. Oxford University Press

Skilling J., 2004, in Fischer R., Preuss R., Toussaint U. V., eds, *American Institute of Physics Conference Series* Vol. 735 of *American Institute of Physics Conference Series*, Nested Sampling. pp 395–405

Suyu S. H., Marshall P. J., Hobson M. P., Blandford R. D., 2006, *MNRAS*, 371, 983

Thomas J., Jesseit R., Naab T., Saglia R. P., Burkert A., Bender R., 2007, *MNRAS*, 381, 1672

Toomre A., 1977, in Tinsley B. M., Larson R. B., eds, *Evolution of Galaxies and Stellar Populations* Mergers and Some Conse-

quences. p. 401

Treu T., Gavazzi R., Gorecki A., Marshall P. J., Koopmans L. V. E., Bolton A. S., Moustakas L. A., Burles S., 2008, *ApJ*, in press

Treu T., Koopmans L. V. E., 2002, *ApJ*, 575, 87

Treu T., Koopmans L. V. E., 2003, *MNRAS*, 343, L29

Treu T., Koopmans L. V. E., 2004, *ApJ*, 611, 739

van de Ven G., Falcon-Barroso J., McDermid R. M., Cappellari M., Miller B. W., de Zeeuw P. T., 2008, preprint (arXiv:0807.4175)

Vegetti S., Koopmans L. V. E., 2008, *MNRAS*, in press

Verolme E. K., de Zeeuw P. T., 2002, *MNRAS*, 331, 959

White S. D. M., Frenk C. S., 1991, *ApJ*, 379, 52